JOURNAL OF MATERIALS SCIENCE 28 (1993) 5469–5478

Microstructural characterization of CO_2 laser welds in the Al–Li based alloy 8090

I. R. WHITAKER, D.G. McCARTNEY
Department of Materials Engineering and Materials Design, University of Nottingham, University Park, Nottingham NG7 2RD, UK

N. CALDER
British Aerospace Defence Ltd, Military Aircraft Division, Samlesbury, Blackburn BB2 7LF, UK

W. M. STEEN
Department of Mechanical Engineering, University of Liverpool, P.O. Box 147, Liverpool L69 3BX, UK

The microstructural development of the Al–Li–Cu–Mg–Zr alloy 8090 has been studied after autogenous CO_2 laser welding. Sheets ranging in thickness from 1–4 mm were welded at speeds of between 20–120 mm s^{-1} and powers from 1.5–3.8 kW. Optical microscopy, scanning and transmission electron microscopy were used to study the as-received base metal, the heat-affected zone and the solidified fusion zone. The base metal was supplied in a superplastically formable condition and thus had an unrecrystallized grain structure containing 1–2 μm sized sub-grains with sub-micrometre δ′ and β′ precipitates in the matrix. In the fusion zone, the as-solidified grain structure was columnar at the interface with the base metal but became equiaxed in the central region of the weld pool. The weld depth and top bead width both increased with decreasing welding speed and increasing beam power within the limits investigated. The fusion zone microstructure was cellular-dendritic. Intermetallic precipitates, which are rich in copper, magnesium, silicon (and presumably lithium), formed in the cell/dendrite boundaries. Very fine-scale δ′ precipitates were present in the as-solidified α-Al matrix but there was no evidence for the β′, S′ and T_1 phases. The heat-affected zone was only 100 μm wide and was characterized by regions of partial melting. Radiographs of welds reveal that porosity occurred predominantly along the weld centre-line. In partial penetration welds, two types of pores were observed: near spherical and irregular. However, in fully penetrating welds, only the spherical type of porosity was present. Overall volume fractions of porosity were measured from metallographic sections and were found to vary with welding speed and weld type, i.e. partial or full penetration.

1. Introduction

In recent years there has been extensive research on the development of Al–Li based alloys for aerospace applications. This has arisen because of their increased moduli and decreased densities compared with conventional 2000 and 7000 series aluminium alloys [1–3]. The Al–Li–Mg–Cu–Zr alloy 8090, with its combination of high specific modulus, high specific strength and acceptable ductility and fracture toughness [1, 3] is finding applications in airframe structures where mechanical fastening is used [4]. However, in view of the superplastically formable capability of 8090 [5] the number of potential aerospace applications would be significantly increased if it could be successfully welded. This is highly desirable, given the much higher cost of Al–Li alloys compared with that of conventional aluminium alloys [4].

It is well known that the high-strength age-hardenable alloys from the 2000 and 7000 series generally have poor weldability when conventional methods are used. Recent reviews [4–7] have indicated that difficulties such as hot cracking and weld porosity were also encountered when filler alloys were employed in either gas–metal or gas–tungsten arc welding of Al–Li based alloys. However, welding with high energy-density heat sources, such as electron beams or lasers, at high welding speeds can eliminate the need for a filler alloy, reduce the heat input to the workpiece, give a fine-scale, rapidly solidified weld pool microstructure and minimize weld cracking. Indeed there have been several reports [7–11] of laser- and electron-beam welding of Al–Li based alloys which have indicated that autogenous keyhole-type welding (typical of a high energy-density beam) leads to a reduction in both porosity and hot-cracking.

The main aim of the present study was to obtain a detailed characterization of the structure which developed in the solidified weld pool and the heat-

0022–2461

affected zone (HAZ) following high-power CO_2 laser welding of 8090 sheet. The term "structure" is used in a broad sense to include grain structure, dendritic structure, interdendritic segregation and sub-micrometre precipitation, as well as porosity formation. The important reasons for undertaking this work were (a) to optimize welding parameters, and (b) to enable post-weld thermal treatments, such as solution treatment and ageing, to be correctly specified in order to obtain desired mechanical properties in the fusion and heat-affected zones.

2. Precipitates in Al–Li–Cu–Mg–Zr alloys

The chemistry of the Al–Li–Cu–Mg–Zr alloy 8090 has been developed to produce precipitation strengthening phases and a dispersoid phase in the α-Al matrix after suitable thermomechanical processing. Quist and Narayanan [12] and Gregson and Flower [13] have reviewed the nature of the microstructural development. The precipitates δ′ (Al_3Li), S′ (Al_2CuMg) and T_1 (Al_2CuLi) form during low-temperature ageing of a supersaturated solid solution whilst the dispersoid β′ ($ZrAl_3$) precipitates out of the matrix during homogenization above 450°C. δ′ (Al_3Li) has a cubic $L1_2$ superlattice structure [14] and forms coherently with a cube/cube orientation relationship with the matrix. Two different δ′ morphologies have been documented, namely small discrete spherical particles and larger particles which appear to nucleate on a core of β′ ($ZrAl_3$) [15]. β′ also forms as a coherent precipitate with an $L1_2$ type superlattice and is metastable, whilst the equilibrium β ($ZrAl_3$) phase has a body centred tetragonal unit cell [16, 17].

Both S′ (Al_2CuMg) and T_1 (Al_2CuLi) are semi-coherent phases. T_1 forms as platelets on $\{1\,1\,1\}_{Al}$ habit planes, whereas S′ exists as laths on $\{2\,1\,0\}_{Al}$ planes [18, 19]. Nucleation of both these phases normally occurs heterogeneously after extended ageing, whereas δ′ appears to form homogeneously. Indeed very fine δ′ is reported to form even in the as-quenched supersaturated solid solution [13].

3. Experimental procedure

The nominal composition of the 8090 used in this study is given in Table I. Laser welding was performed on sheets of various thicknesses ranging from 1–4 mm. The sheet was supplied in an unrecrystallized condition, generated by a proprietary thermomechanical treatment, with a microstructure suitable for superplastic forming (SPF). This is termed the as-received, SPF condition. All sheets were degreased prior to welding, and in some cases the surfaces were chemically etched to remove surface oxide. The latter process was carried out by immersing the sheet in 30% NaOH and rinsing in dilute HNO_3, followed by water and alcohol, before drying.

TABLE I Nominal composition of alloy 8090 (wt%)

Element	Li	Cu	Mg	Zr	Al
%	2.4	1.1	0.6	0.1	Bal.

Laser welding was conducted with either a Ferranti 5 kW or an Electrox 2 kW CO_2 laser. Both lasers produced a continuous wave output at 10.6 μm. The laser beam was focused on to the sheet surface using a 120 mm focal length KCl lens. The output beam was circular in cross-section with an approximately Gaussian energy distribution and diameter of 0.25 mm. Autogenous bead on plate welds were performed at power levels ranging from 1.5–3.8 kW and at speeds from 20–120 mm s^{-1}. A coaxial helium gas flow was employed at a flow rate of typically 40 l min^{-1}.

Optical microscopy was performed on planes perpendicular and parallel to the welding direction, and the three mutually perpendicular planes are defined in Fig. 1. Final polishing of metallographic sections was with Struers OP-S colloidal silica on a soft cloth. Etching was carried out using Kellers Reagent [20] or 10% NaOH at room temperature followed by a rinse in dilute HNO_3. In addition, anodizing in Barker's Reagent [20] also revealed the grain structure when viewed under crossed-polars in an optical microscope.

In order to quantify weld porosity, a technique was developed for sectioning accurately along longitudinal planes (see Fig. 1). The bead on plate weld was mounted in bakelite and held in a jig which enabled the weld depth profile and included porosity to be measured on a longitudinal plane and repeated at intervals of approximately 50 μm through the thickness of the weld. Approximately 9 mm long sections from welds could be examined using this technique, and for each longitudinal plane section the total weld area and area of porosity were measured using an automatic image analysis system. By examining a sufficient number of closely spaced longitudinal planes it was possible to determine the total volume fraction of porosity in each length of weld examined. In addition, the nature and morphology of pores were investigated using scanning electron microscopy (SEM).

Samples for transmission electron microscopy (TEM) were taken from sections parallel to the rolling plane and approximately 1 mm from the surface of the weld or as-received sheet. The bulk sample was, in each case, ground to a thickness of approximately 500 μm and 3 mm diameter discs were then punched out of this. After further grinding to approximately 300 μm, thin foils were obtained through twin jet electropolishing in a solution of 25% nitric acid in methanol at − 30 °C and 15–20 V. TEM was conducted at 120 kV on a Philips EM400T.

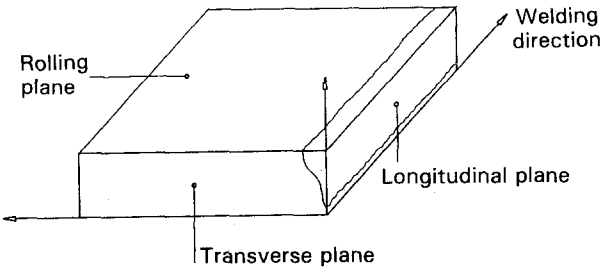

Figure 1 Illustration of the orientation of the three mutually perpendicular planes from which metallographic sections were taken.

Qualitative compositional analysis was performed on both the SEM and TEM using energy dispersive X-ray analysis (EDAX). This technique cannot, of course, detect lithium.

Macro- and micro-Vickers hardness measurements were performed on as-received base metal, heat-affected zones and weld metal using standard procedures.

4. Results

4.1. Microscopy of the base metal

An optical micrograph of unetched base metal is shown in Fig. 2a, and this reveals that the as-received, SPF condition, base metal consisted of an aluminium matrix together with a number of intermetallic phases. Using EDAX on the SEM, the following types of intermetallic phase were found: (i) a widespread, flaky phase measuring approximately 2 μm × 10 μm and containing aluminium, magnesium and copper, (ii) a dispersion of a globular phase around 2 μm diameter and containing aluminium, magnesium, iron and copper, and (iii) an occasional 20 μm size phase containing aluminium, zirconium, titanium and copper. These phases might also, of course, have contained lithium which cannot be detected by EDAX analysis. After anodizing, and when viewed under polarized light, the grain structure was found to be unrecrystallized. Furthermore TEM, Fig. 2 (b), showed that 1–2 μm sized sub-grains were present within the unrecrystallized grains. Sub-micrometre precipitates were also present within the sub-grains and TEM dark-field imaging from the δ′ superlattice diffraction spots revealed that this phase had a bimodal size distribution as shown in Fig. 3. There was a distribution of fine-scale δ′ precipitates, approximately 15 nm diameter, together with larger precipitates up to 100 nm diameter. The latter were found to exhibit a core of reduced contrast using the dark-field (DF) imaging conditions of Fig. 3. The core was found to be zirconium rich, 20–50 nm diameter, and hence presumably the coherent, metastable form of $ZrAl_3$ (β′). In addition to the β′ and δ′ phases, a further blocky precipitate, approximately 100 nm in size, can be seen in the matrix under bright-field conditions, and Fig. 4 shows examples of such precipitates. EDAX showed this precipitate phase to contain principally aluminium and zirconium with lesser amounts of copper and titanium, and was

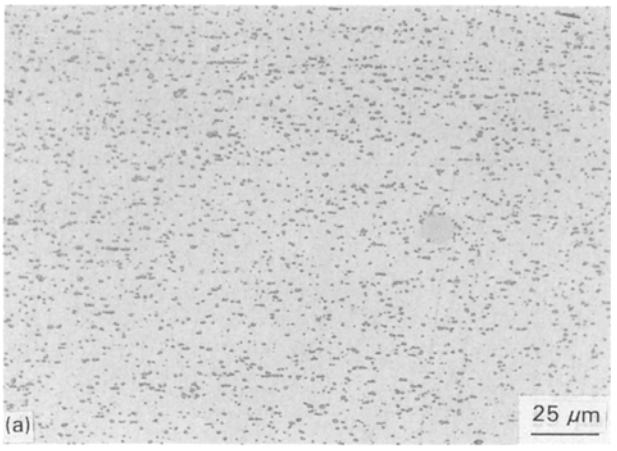

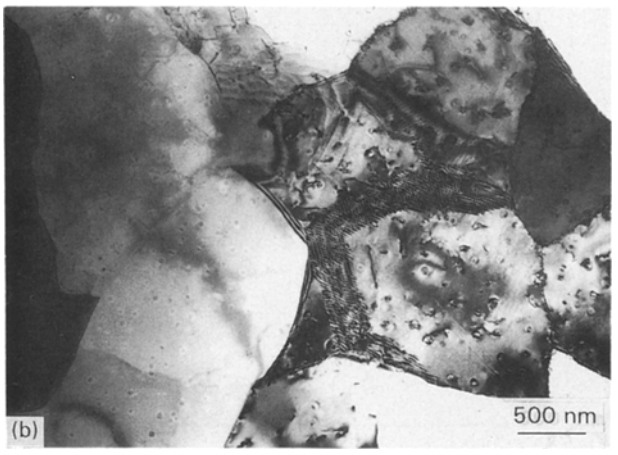

Figure 2 (a) Optical micrograph of 8090 base metal in the unetched condition and taken from a transverse plane. Intermetallic phases are seen in the aluminium matrix; (b) A transmission electron micrograph of 8090 base metal in the as-received condition showing the sub-grain structure.

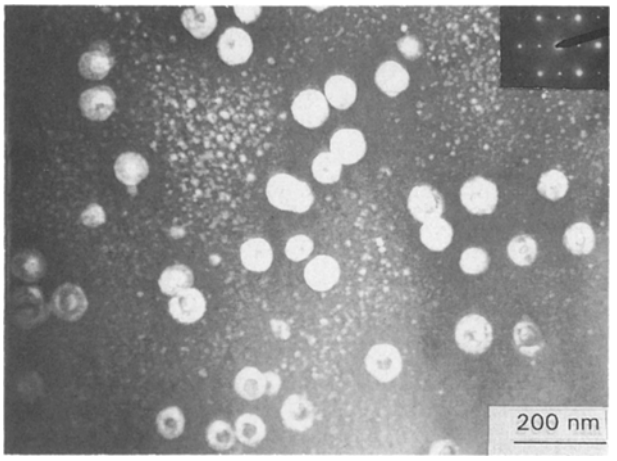

Figure 3 As-received 8090 base metal. Dark-field transmission electron micrograph using a δ′ superlattice reflection from a [0 1 1] zone axis orientation. Homogeneous δ′ and composite δ′/β′ precipitates are visible. The inset shows the corresponding selected-area diffraction pattern.

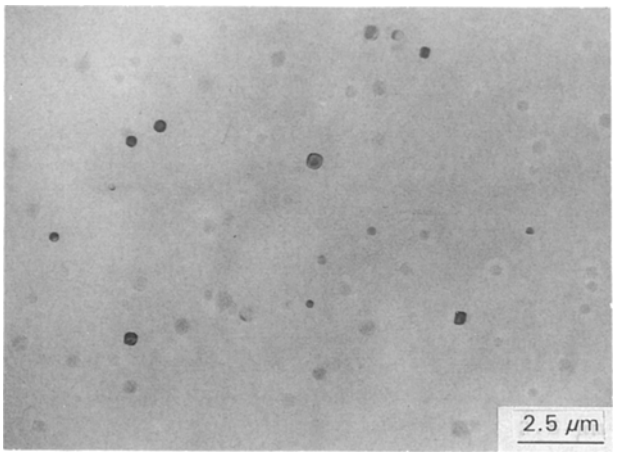

Figure 4 Transmission electron micrograph of 8090 sheet in as-received condition. Bright-field image close to a [0 0 1] zone axis. Faint contrast from δ′ and β′ can be seen with strong contrast from blocky precipitates, identified as tetragonal $ZrAl_3$.

identified as the equilibrium tetragonal form of $ZrAl_3$ using selected-area electron diffraction patterns.

4.2. Weld dimensions and grain structure

As expected, the laser beam power and the welding speed influence the size and shape of the weld. The graphs in Fig. 5 a and b summarize the effects of beam power and welding speed on weld top bead width, w, and weld depth, d, i.e. penetration in 3.2 mm 8090 sheet. Fig. 5a is for a fixed speed of 100 mm s^{-1} whilst Fig. 5b was obtained for a power of 2.1 kW. The parameters w and d were largely unaffected by the flow rate of the helium shielding gas. An important point to note is that keyholing was obtained at much lower powers and power densities than is normally possible with conventional aluminium alloys.

The overall shape and grain structure of a solidified autogenous bead-on-plate weld is shown in Fig. 6 for a partial penetration weld in 3.2 mm sheet. The profile of the weld cross-section (Fig. 6a) is characteristic of that for deep-penetration keyhole welding and has variously been described as "wine cup" or "nail head" in shape. The as-solidified grain structure, revealed by anodizing, is seen to be complex. Fine columnar grains have developed around the edges of the weld, and an equiaxed morphology has formed in the lower region of the weld pool. However, in the upper region of the pool a coarse columnar structure formed with the appearance of a coarse equiaxed region towards the centre-line, Fig. 6b. Fig. 6c reveals marked banding of the grain structure combined with periodic variations in penetration. The grain morphologies, sizes and distributions were relatively insensitive to the welding conditions. The porosity observable in Fig. 6 will be described in detail in a subsequent section. Weld cracks were only occasionally observed and these ran perpendicular to the welding direction, close to the top surface.

4.3. Microstructure of the weld metal

The microstructure of the solidified weld metal is shown in Fig. 7. It is clear from Fig. 7a that the fusion boundary consisted of a very narrow band of almost globular, non-dendritic grains which separated the weld pool from the rest of the heat-affected zone (HAZ). The HAZ width was less than 150 μm and contained small intergranular regions with a star-shaped morphology typical of localized grain-boundary melting. The microhardness of the HAZ was 100 kgf mm^{-2} as compared to 80 kgf mm^{-2} for the base material. The microstructure in the central region of the lower part of the weld is shown, in Fig. 7b, to consist of cellular or dendritic equiaxed grains of various sizes. The interdendritic phases which formed were examined in greater detail using TEM, and Fig. 8a shows cells or dendrite arms of the α-Al together with the interdendritic phases. Semi-quantitative EDAX analysis showed the α-Al to be depleted in copper and magnesium at the cell/dendrite arm centre and enriched in these elements at the edges. The

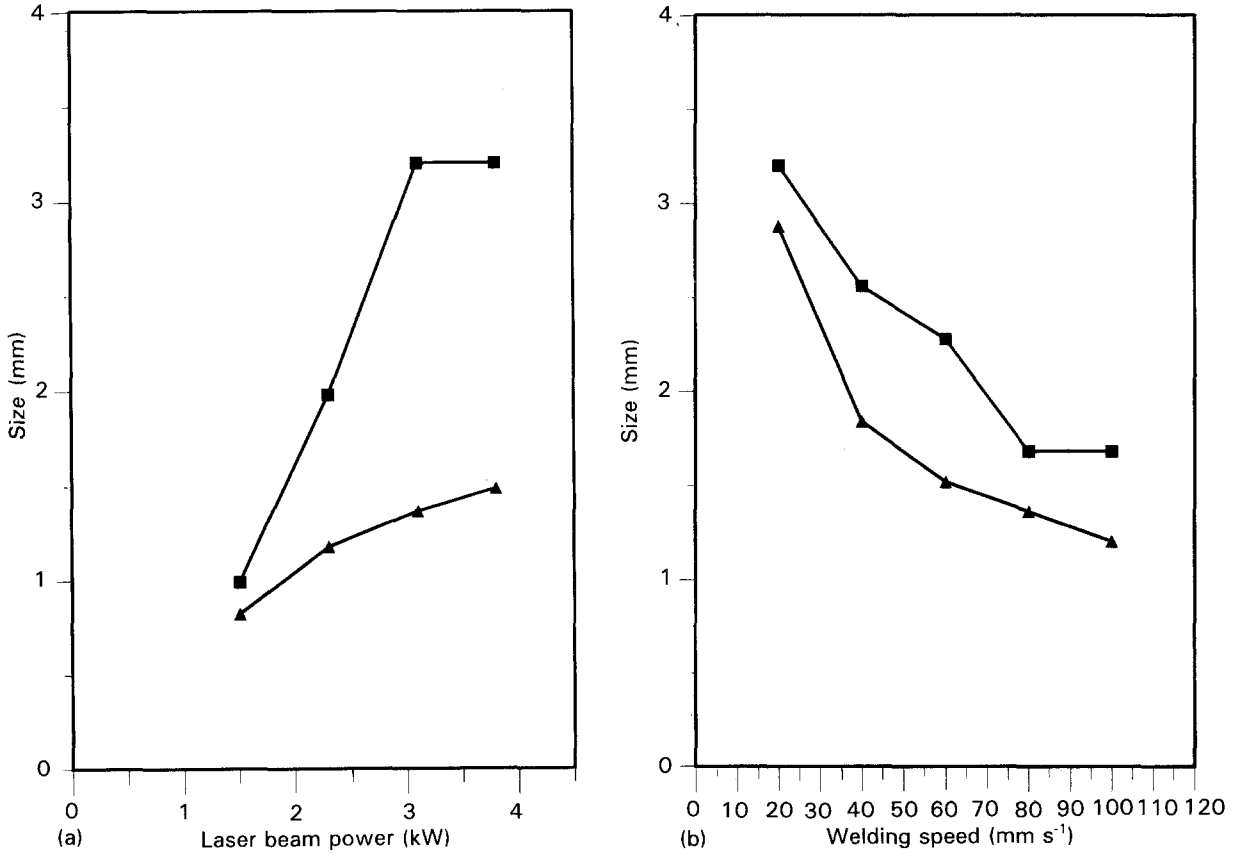

Figure 5 Graphs showing the effect of welding parameters on (▲) weld top bead width, w, and (■) penetration, d, for 3.2 mm sheet. (a) The variation of w and d with incident laser beam power at 100 mm s^{-1} welding speed; (b) the variation of w and d with welding speed at 2.1 kW laser beam power.

EDAX spectrum shown in Fig. 8b was taken from the interdendritic material and showed it to be enriched in copper, magnesium, silicon and iron. Two separate crystalline phases were identified in interdendritic regions, but it has not yet been possible to determine their crystal structures. The δ′ phase was also present in the as-solidified weld as a very fine precipitate within the α-Al matrix. The δ′ particles could only just be imaged because of their small size, as shown in the transmission electron micrograph of Fig. 9. The β′ phase did not appear to form in the as-soldified α-Al matrix.

4.4. Assessment of porosity

Radiographs of bead on plate welds confirmed that large pores were situated predominantly along the weld centre-line, i.e. the region which would have been traversed by the vaporized region known as the key-hole [21].

In partial penetration welds, two different types of pores could be clearly identified as shown in Fig. 10. The near-spherical pore of Fig. 10a, in which the dendritic solidification structure was visible on pore walls, will be termed type I porosity. The irregular shaped pores shown in Fig. 10b will be termed type II porosity. They did not reveal solidification structures on the pore walls, and instead appeared to possess a complex folded type of structure characteristic of cold-shuts in conventional castings [22]. In full penetration welds, type II porosity was virtually absent.

Using the technique described in the Section 3, measurements were made of area fraction of porosity on longitudinal plane sections. Fig. 11 shows macrophotographs of four successive longitudinal plane sections taken from a partial penetration weld in 4 mm

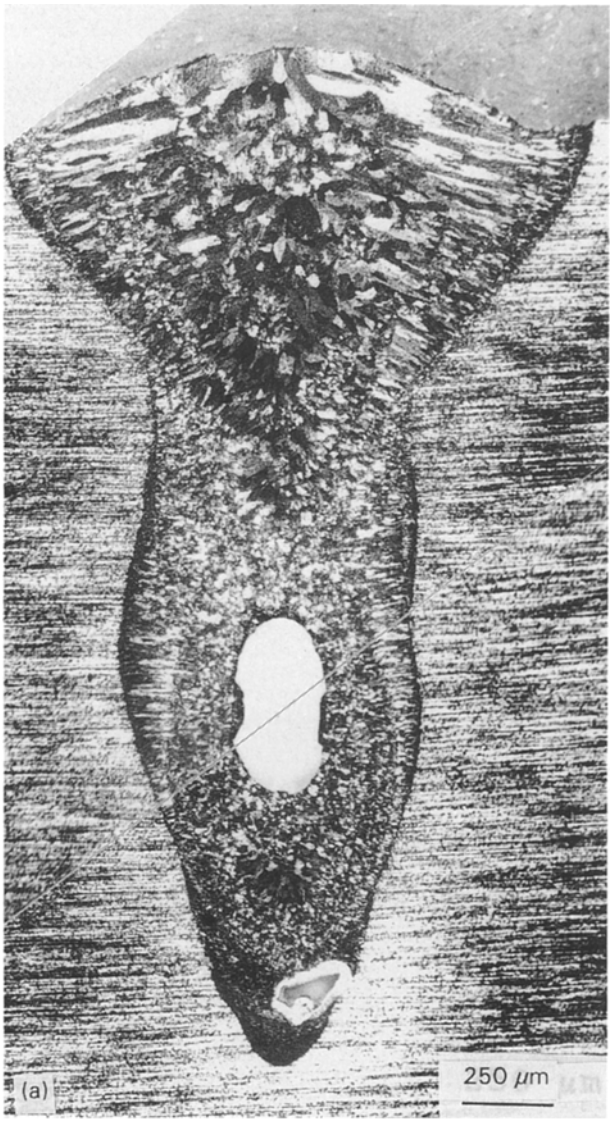

Figure 6 Optical micrographs showing the grain structure of a partial penetration weld in 3.2 mm sheet (3.1 kW, 100 mm s^{-1}). Anodized structures viewed under polarized light: (a) a transverse plane, (b) a rolling plane close to the top surface, and (c) a longitudinal plane along the weld centre-line. Porosity is also visible in (a) and (c).

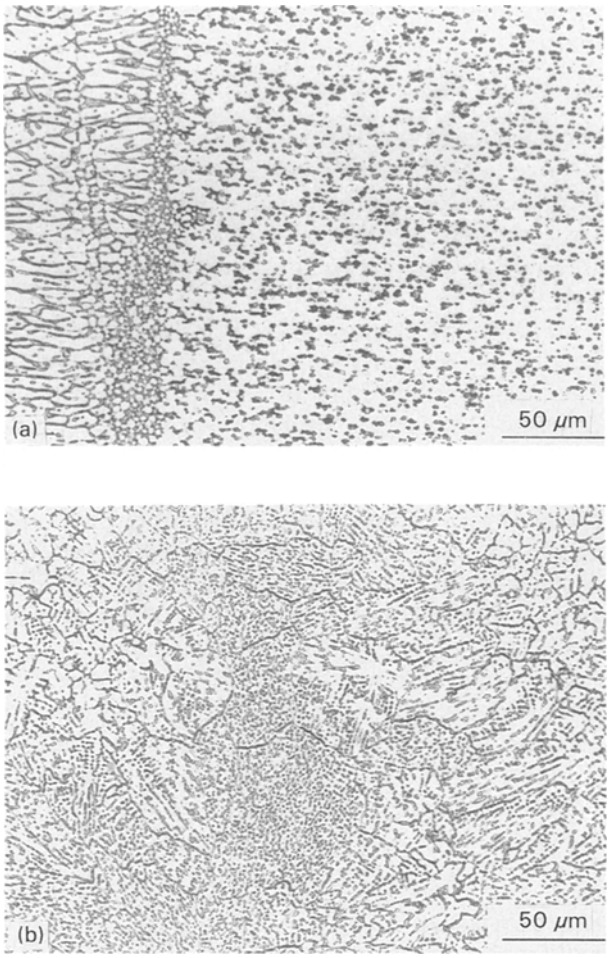

Figure 7 Etched transverse section of a partially penetrating weld showing (a) a region close to the fusion boundary, and (b) the interior of the weld close to the centre-line. $V = 60$ mm s^{-1}. In (a) the partially melted heat-affected zone is to the right of the micrograph.

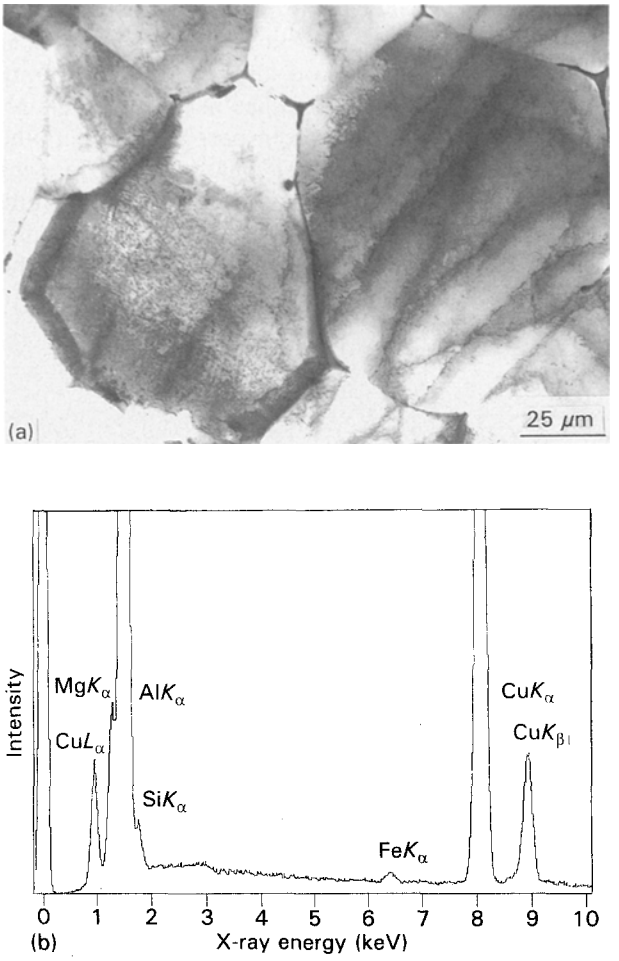

Figure 8 (a) Transmission electron micrograph of the weld solidification structure and (b) the EDAX spectrum from the interdendritic regions.

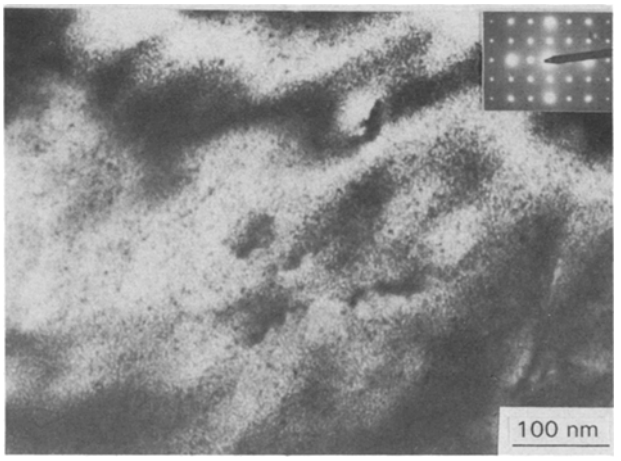

Figure 9 Bright-field transmission electron micrograph taken along the [0 0 1] aluminium zone axis of the as-solidified weld showing a very fine-scale precipitation of the δ′, together with the zone axis diffraction pattern (inset).

sheet. It can be seen that the porosity was concentrated in the lower part of the weld and its area fraction decreased quite rapidly with distance from the centreline. The graph in Fig. 12 displays the results for two welding speeds which both gave partial penetration welds. From data of this type the total volume fraction of porosity in selected weld lengths was calculated and Table II summarizes the results obtained. Generally the fraction of porosity decreased with increasing welding speed at a fixed power input, and the transition from partial to full penetration also led to a reduction in porosity. In all these experiments the beam power and focus position were unchanged. The chemical etching employed was found to have little effect on overall levels of porosity.

5. Discussion

The purpose of this discussion is to address two areas namely the development of the alloy microstructure after welding and the formation of porosity in the weld pool. Hence these topics will be considered separately.

5.1. Effect of welding thermal cycle on microstructure

The precise thermomechanical processing route for developing, in 8090, the fine-grain microstructure for superplasticity remains a proprietary process [23, 24]. However, Pilling and Ridley [25] have outlined the important stages as being overageing at around 400 °C followed by warm working around 200 °C. The intermetallic precipitates seen in Fig. 2 are certainly consistent with an overageing heat treatment and qualitatively their compositions, as revealed by

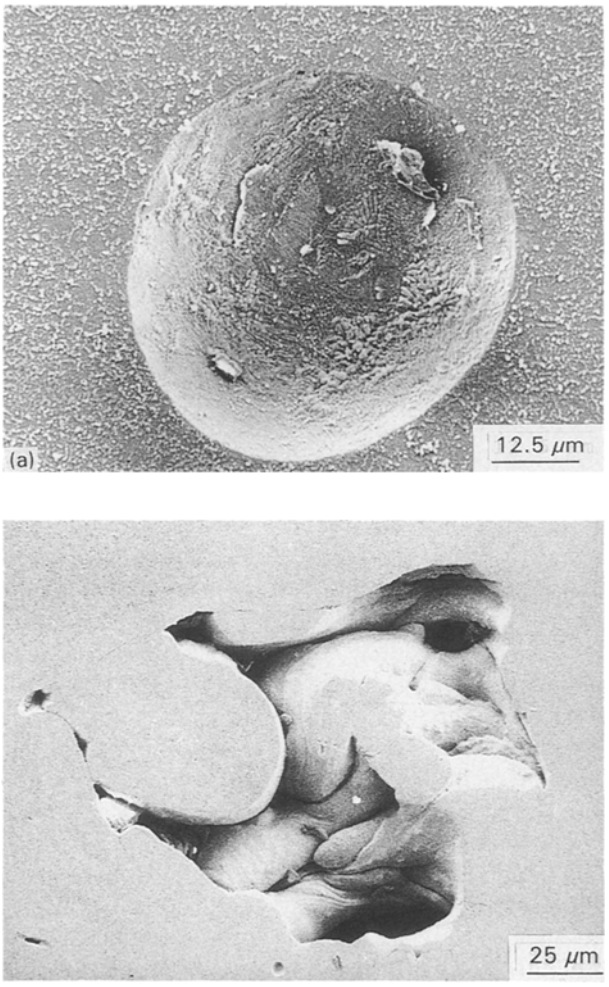

Figure 10 Scanning electron micrographs illustrating the different forms of porosity in a partially penetrating weld. A regular spherical pore is shown in (a), and (b) shows a typical example of an irregular pore with folds of metal.

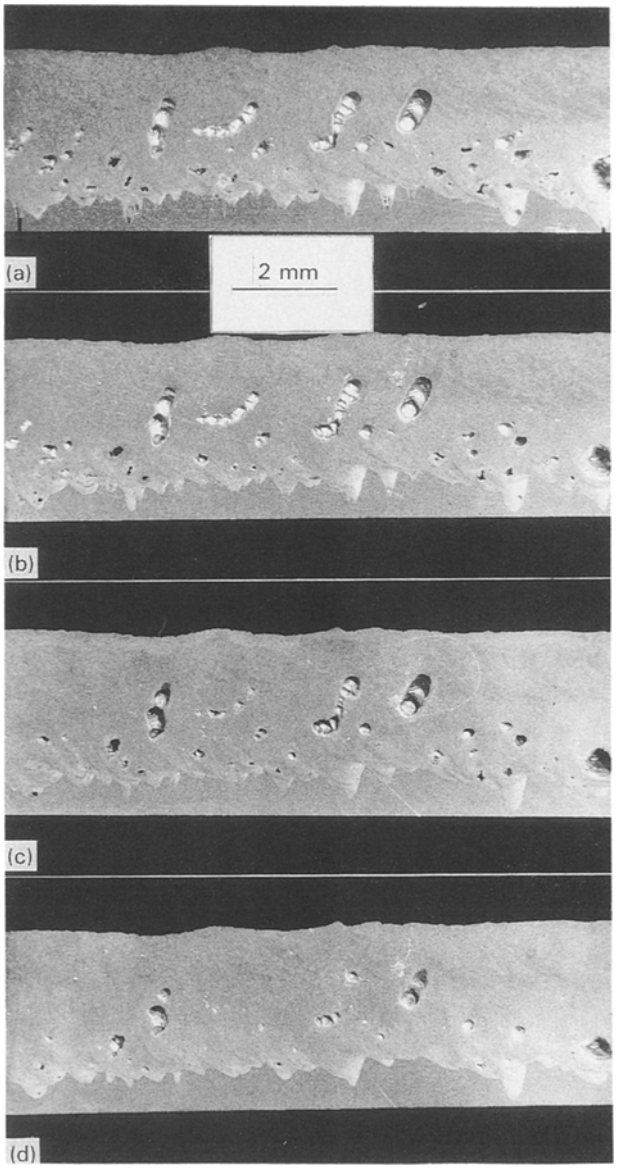

Figure 11 Macrophotographs of longitudinal planes in a partially penetrating weld. The plane shown in (a) was very close to the weld centre-line whilst (b–d) were from planes 50, 100 and 150 μm from (a) respectively.

EDAX, are similar to those reported by Pandey *et al.* [26] who examined intermetallic particles in an Al–Li based superplastic alloy of similar composition. The bimodal δ′ size distribution, with β′ cores to the larger δ′ precipitates, was a characteristic feature of the base metal with neither S′ nor T_1 phases being observed. The δ′ precipitate presumably formed during air cooling after warm working, whereas the β′ phase would have precipitated during ingot homogenization prior to thermomechanical processing. It is, however, unclear at which stage the equilibrium tetragonal β phase, seen in Fig. 4, would have formed. Although the base metal contained unrecrystallized α-Al grains there were, within these, sub-grains 1–2 μm in size. Shakesheff *et al.* [27] have reported that a fine stable grain size develops from these sub-grains during the initial stages of superplastic forming.

The grain structure of the solidified fusion zone was very different from that of the base metal and varied considerably from one part of the weld cross-section to another as shown in Fig. 6. At the interface with the base metal columnar grains are seen to form and grow into the weld pool with what appears to be epitaxial growth on pre-existing solid grains at the fusion boundary. In the lower part of the weld, associated with the near parallel sided keyhole, columnar growth was rapidly terminated and a fully equiaxed grain structure developed giving a relatively fine equiaxed grain size. In the upper, or "wine cup", portion of the weld columnar growth predominated with the orientation of the columnar grains changing continually whilst attempting to follow the heat flow field. However, towards the weld centre line the structure did become equiaxed with much larger equiaxed grains than in the lower part of the keyhole. Clearly, without detailed numerical calculations for the temperatures and flow fields within the keyhole it is only possible to consider, in a qualitative fashion, the differences in grain structure within the weld. The columnar to equiaxed transition is known to be promoted by a number of factors including a low-temperature gradient in the melt, high solidification-front velocity, fluid flow in the melt, and the presence of heterogeneous nucleating particles [28]. The number density of nucleating particles is unlikely to vary from one part of the weld pool to another and so it is most probably

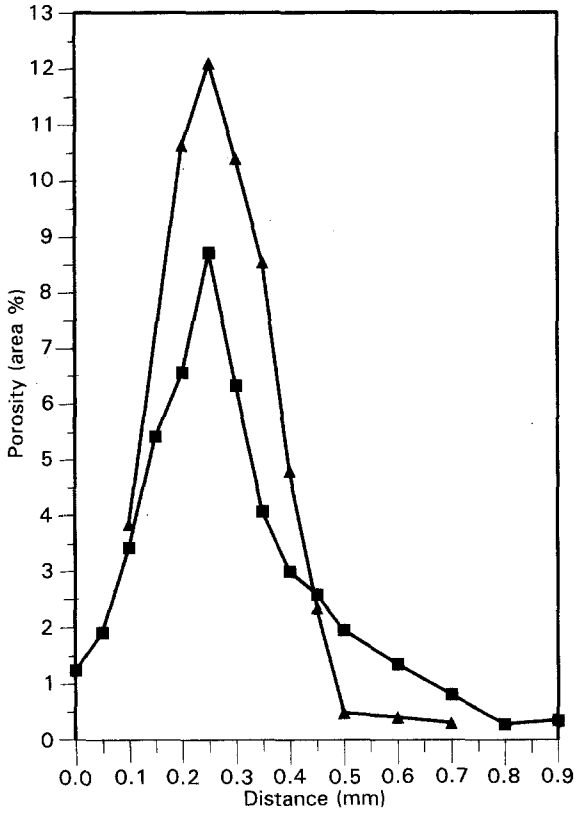

Figure 12 Plot showing porosity area fraction versus longitudinal plane position (arbitrary origin) for two welding speeds: (▲) 60 mm s^{-1}, (■) 100 mm s^{-1}. Beam power 2 kW, sheet thickness 4 mm, surface focus.

TABLE II Variation of porosity with welding conditions for a power input of 2 kW

Welding speed (mm s^{-1})	Sheet thickness (mm)	Weld penetration	Porosity (Vol %)
60	2	Full	0.39
	3.2	Full	0.28
	4	Partial	3.04
100	3.2	Partial	1.10
	4	Partial	2.30

changes in fluid and heat flow conditions which are responsible for the different grain structures with the pronounced columnar structure in the upper part of the weld, perhaps indicating that melt-temperature gradients were significantly higher there.

Fig. 7 reveals that the dendritic microstructure within the weld pool is characterized by secondary dendrite arm spacings of the order of 2–5 μm which would imply that local solidification times are of a second or less [29]. These values are similar to those obtained from measurements performed by Sonti and Amateau [30] on laser-welded non-lithium containing aluminium alloys of otherwise similar composition. Because the non-equilibrium freezing range of 8090 is in excess of 100 K, this would indicate cooling rates through the semi-solid state of more than 100 K s^{-1}. The microstructure close to the fusion boundary is particularly interesting in that it consists of a band of globular grains of α-Al whose sizes are around 1–5 μm as shown in Fig. 7a. It is probable that the globular α-Al developed during the heating cycle, as the high-intensity beam traversed the material, and its formation could be explained as follows. Close to the fusion boundary there will be material which has been briefly heated into the semi-solid state with the fraction of liquid forming at any location being dependent on the temperature reached. Initial melting will occur at grain boundaries, but once sufficient liquid has formed it will be capable of wetting the sub-grain boundaries providing the sub-grain boundary energy is greater than twice the solid–liquid surface energy. Such a mechanism would account for the spatial scale of the globular α-Al (because 1–2 μm sized sub-grains are present in the base metal) and has, in fact, been observed to occur [31], in stir-cast aluminium alloys.

Because the heat-affected zone is only of the order of 100 μm wide, it has not been possible to carry out a detailed TEM examination of this region. Thus TEM analysis has been confined to the as-solidified fusion zone. The microsegregation within the α-Al was consistent with that expected for copper and magnesium whose partition coefficients are both much less than 1. The plate-like precipitates, which were present in interdendritic regions, have not been fully characterized. However, their presence is not unexpected, in that precipitates of similar compositions have been found in rapidly solidified, melt-spun ribbons of Al–Li based alloys [32]. In these ribbons the precipitates were identified as having an icosahedral structure, but this appears not to be so for the intermetallic phases shown in Fig. 8a which undoubtedly formed as second phases in a solidification reaction. Furthermore very fine-scale δ′ precipitate particles were observed in the α-Al matrix as revealed by Fig. 9. This observation is consistent with reports which showed δ′ formation during solid-state quenching from the single-phase α-Al region [13] and also during rapid quenching from the melt [32].

5.2. Formation of porosity in the weld pool

With regard to porosity, it is important to emphasize that two different types of pore were identified as illustrated in Fig. 10. The type I or spherical pores occurred in both partial and full penetration welds, whereas the irregular pores, termed type II, were confined to partial penetration welds. The concentration of porosity close to the weld centre-line is confirmed by the sequence of micrographs in Fig. 11 as is the connectivity of the pores.

Considering firstly type I pores, they were, in general, much larger than the cell/dendrite arm spacings and were characterized by (a) having a dendritic solidification pattern visible on their internal surface, and (b) being nearly spherical. Previous studies on laser-welded Al–Li based alloys [7, 11] have also reported spherical porosity, and pores are, of course, a common feature of gas–tungsten arc aluminium alloy weldments [33]. In the light of previous observations [33] it seems certain that hydrogen gas is the underlying cause of the type I pores. Hydrogen can readily be absorbed into molten aluminium from surface contaminants but the precise mechanism whereby large

spherical gas pores nucleate and grow during solidification is not well understood. However, the fundamental thermodynamic driving forces are (a) a decrease in equilibrium hydrogen solubility with decreasing temperature of the melt and (b) a much lower hydrogen solubility in solid than in liquid at the solidification temperature. Devletian and Wood [33] have noted that in molten aluminium the maximum to minimum hydrogen solubility in the melt is approximately 70, whilst Talbot [34] has reported liquid to solid solubility ratios of 29 and 3 for pure aluminium and Al–2 wt % Li alloys, respectively. Hence both these factors will provide a strong driving force for hydrogen gas bubble nucleation.

In view of the irregular morphology of type II pores (Fig. 10b) it is probable that their formation is related to the keyhole dynamics of a partial penetration weld [21]. The precise mechanism involved is clearly complex, but it may well be caused by irregular evaporation mechanics on the leading edge of the keyhole. This has been shown by Arata [35] to cause a burst of vapour from the surface of the keyhole horizontally back into the trailing melt pool. This may form a bubble within the lower section of the weld pool. Under certain circumstances this may be trapped and lead to cold-shut formation. Arata, using in-process optical and X-ray analysis, observed laser welding of soda–lime glass and mild steel [35]. The pattern reported is very similar to that seen in Fig. 11. Furthermore, similar spiking effects have been observed in electron-beam welding [36, 37]. Shauer and Giedt [37] have examined the balance between surface tension and vapour pressure forces within the keyhole and predicted that instabilities will form at the depth where the surface tension force just exceeds that due to the vapour pressure. Because both forces are temperature dependent, further calculations would require a detailed knowledge of the keyhole temperature profile. Clearly, though, cavity instability provides a possible mechanism for the formation of entrapped porosity and uneven penetration which are the characteristic features revealed in Fig. 11. The influence of welding speed on volume fraction of porosity (in partial penetration welds) could therefore, in part, be due to its effect on both melt-pool temperatures and trailing melt-pool size, which will determine keyhole stability. Finally, Table II reveals a marked decrease in porosity in going from partial to fully penetrating welds. Microstructural observation has confirmed that this is associated with the elimination of type II (irregular) pores once a keyhole is established which goes through the material's thickness. In the full penetration case, vapour entrapment is much less likely to occur.

6. Conclusions

1. The Al–Li based alloy 8090 can be welded using a CO_2 laser at power levels in the range 1.5–3.8 kW, and speeds from 20–120 mm s^{-1}.

2. The microstructure of the solidified fusion zone consists of columnar grains close to the fusion zone boundary and equiaxed grains towards the weld centre line. The grain size is found to be significantly finer, with a more extensive equiaxed region, in the lower part of the weld.

3. Secondary dendrite arm spacings in the fusion zone are typically 2–5 μm and second-phase particles are found to occur interdendritically. These particles are rich in copper, magnesium, iron and silicon, and probably also contain lithium. There is also segregation of copper and magnesium within the aluminium dendrites due to non-equilibrium solidification.

4. Fine-scale δ′ precipitates within the α-Al of the fusion zone during laser welding, but there was no evidence for precipitation of β′, S′ or T_1.

5. The width of the heat-affected zone is approximately 100 μm and its hardness is around 100 kgf mm^{-2} compared to 80 kgf mm^{-2} for as-received SPF grade base material. Fine globular grains of α-Al are found at the fusion zone boundary with the base metal.

6. Porosity is found predominantly along the weld centre-line and two types are observable in partial penetration welds. The spherical, type I, pores are attributed to hydrogen gas evolution, whereas the irregular type II pores are believed to form because of keyhole instability. In full penetration welds, the latter type are virtually absent.

Acknowledgements

This work was supported by the Science and Engineering Research Council and British Aerospace through a Co-operative Research Grant and CASE award research studentship.

References

1. R. GRIMES, A. J. CORNISH, W. S. MILLER and M. A. REYNOLDS, *Met. Mater.* **1** (1985) 357.
2. P. E. BRETZ and R. G. GILLILAND, *Light Met. Age* **45** (3–4) (1987), 7.
3. A. J. CORNISH, A. GRAY, W. S. MILLER and M. A. REYNOLDS, in "Proceedings of the 3rd European Symposium on Spacecraft Materials in Space Environment", Noordwijk, Netherlands, 1985, pp. 195–201.
4. J. R. PICKENS, *J. Mater. Sci.* **25** (1990) 3035.
5. R. GRIMES, W. S. MILLER and R. G. BUTLER, *J. Phys. (France)* **48** (1987) C3–239.
6. I. J. POLMEAR, "Light Metals" (Edward Arnold, London, 1981) p. 94.
7. P. A. MOLIAN and T.S. SRIVATSAN, *J. Mater. Sci.* **25** (1990) 3347.
8. D. S. GNANAMUTHU and R. J. MOORES, in E. A. Metzbower and D. Hauser (eds), "Power Beam Processing", (ASM, Metals Park, Ohio, 1989) pp. 181–3.
9. A. J. SUNWOO and J. W. MORRIS, *Metall. Trans.* **22A** (1991) 903.
10. *Idem, Weld. J.* **69** (1989) 262–S.
11. B. BIERMANN, R. DIERKEN, R. KUPFER, A. LANG and H. W. BERGMANN, in "Proceedings of the 6th International Al–Li Conference", October 1991, Garmisch, Germany, to be published.
12. W. E. QUIST and G. H. NARAYANAN, in "Modern Aluminium Alloys", edited by A. K. Vasudevan and R. D. Doherty (Academic Press, New York, 1989) p. 219.
13. P. J. GREGSON and H. M. FLOWER, *Mater. Sci. Technol.* **3** (1987) 81.
14. J. M. SILCOCK, *J. Inst. Met.* **88** (1959–1960) 357.
15. F. W. GAYLE and J. B. VANDERSANDE, *Scripta Metall.* **19** (1984) 473.
16. N. RYUM, *Acta Metall.* **17** (1969) 269.

17. O. IZUM, *ibid.* **17** (1969) 619.
18. R. N. WILSON and P. G. PARTRIDGE, *ibid.* **13** (1965) 1321.
19. W. A. CASSADA, G. J. SHIFLET and E. A. STARKE, *Metall. Trans.* **22A** (1991), 287.
20. "Metals Handbook", 9th Edn, Vol. 9 (ASM International, Metals Park OH, 1988) pp. 351–88.
21. W. M. STEEN, "Laser Material Processing" (Springer-Verlag, London, 1991) pp. 108–44.
22. G. J. DAVIES, "Solidification and Casting" (Applied Science, London, 1973) pp. 55–67.
23. W. S. MILLER and J. WHITE, in "Superplasticity in Aerospace" (TMS, Warrendale, PA, 1988) pp. 211–28.
24. D. H. SHIN, Y. H. SHIN, Y. W. CHANG and S. C. MAENG, *Scripta Metall. Mater.* **26** (1992) 117.
25. J. PILLING and N. RIDLEY, "Superplasticity in Crystalline Solids" (The Institute of Metals, London 1989) p. 20.
26. M. C. PANDEY, J. WADSWORTH and A. K. MUKHERJEE, *J. Mater. Sci.* **23** (1988) 3509.
27. A. J. SHAKESHEFF, D. S. MCDARMAID and P. J. GREGSON, *Mater. Sci Technol.* **7** (1991) 276.
28. S. C. FLOOD and J. D. HUNT, in "Metals Handbook", 9th Edn, Vol. 15 (ASM International, Metals Park OH, 1988) pp. 130–5.
29. M. C. FLEMINGS, "Solidification Processing" (McGraw-Hill, New York, 1974) p. 150.
30. N. SONTI and M. F. AMATEAU, *Numer. Heat Transf. A* **16** (1989), 351.
31. R. D. DOHERTY, *Mater. Sci. Eng.* **65** (1984), 181.
32. D. H. KIM, B. CANTOR and H. I. LEE, *J. Mater. Sci.* **23** (1988) 1695.
33. J. H. DEVLETIAN and W. E. WOOD, *Weld. Res. Council Bull.* **290** (1983) 1.
34. D. E. J. TALBOT, "Solidification Processing 1987", edited by J. Beech and H. Jones (Inst. of Metals, London, 1988) pp. 29–32.
35. Y. ARATA, in "Proceedings of International Conference on Laser Advanced Materials Processing" (LAMP '87), Osaka, 1987, pp. 3–12.
36. H. TONG and W. H. GIEDT, *Weld. J.* **49** (1970) 259–S.
37. D. A. SCHAUER and W. H. GIEDT, *ibid.* **57** (1978) 189–S.

Received 6 October 1992
and accepted 7 January 1993